AGU PUBLICATIONS

JGR

Journal of Geophysical Research: Space Physics

RESEARCH ARTICLE
10.1002/2017JA024510

Key Points:
- Increased SWARM in situ electron density toward high latitudes in presence of equatorward large-scale TIDs
- Evidence of equatorward TIDs in influencing altitudinal plasma distribution to the topside ionosphere
- Possibility of poleward TIDs launched from the geomagnetic equatorial region with comparable velocity values in both hemispheres

Correspondence to:
J. B. Habarulema,
jhabarulema@sansa.org.za

Citation:
Habarulema, J. B., Yizengaw, E., Katamzi-Joseph, Z. T., Moldwin, M. B., & Buchert, S. (2018). Storm time global observations of large-scale TIDs from ground-based and in situ satellite measurements. *Journal of Geophysical Research: Space Physics*, *123*, 711–724. https://doi.org/10.1002/2017JA024510

Received 27 JUN 2017
Accepted 28 NOV 2017
Accepted article online 7 DEC 2017
Published online 4 JAN 2018

Storm Time Global Observations of Large-Scale TIDs From Ground-Based and In Situ Satellite Measurements

John Bosco Habarulema[1,2], Endawoke Yizengaw[3], Zama T. Katamzi-Joseph[1,2], Mark B. Moldwin[4], and Stephan Buchert[5]

[1]South African National Space Agency, Space Science, Hermanus, South Africa, [2]Department of Physics and Electronics, Rhodes University, Grahamstown, South Africa, [3]Institute for Scientific Research, Boston College, Chestnut Hill, MA, USA, [4]Swedish Institute of Space Physics, Uppsala University, Uppsala, Sweden, [5]Department of Climate and Space Sciences and Engineering, University of Michigan, Ann Arbor, MI, USA

Abstract This paper discusses the ionosphere's response to the largest storm of solar cycle 24 during 16–18 March 2015. We have used the Global Navigation Satellite Systems (GNSS) total electron content data to study large-scale traveling ionospheric disturbances (TIDs) over the American, African, and Asian regions. Equatorward large-scale TIDs propagated and crossed the equator to the other side of the hemisphere especially over the American and Asian sectors. Poleward TIDs with velocities in the range ≈400–700 m/s have been observed during local daytime over the American and African sectors with origin from around the geomagnetic equator. Our investigation over the American sector shows that poleward TIDs may have been launched by increased Lorentz coupling as a result of penetrating electric field during the southward turning of the interplanetary magnetic field, B_z. We have observed increase in SWARM satellite electron density (N_e) at the same time when equatorward large-scale TIDs are visible over the European-African sector. The altitude N_e profiles from ionosonde observations show a possible link that storm-induced TIDs may have influenced the plasma distribution in the topside ionosphere at SWARM satellite altitude.

1. Introduction

Traveling ionospheric disturbances (TIDs) are widely believed as evidence of the presence of atmospheric gravity waves within the ionosphere (e.g., Davis, 1971; Hines, 1960; Georges & Hooke, 1970). They are generally categorized into medium-scale and large-scale TIDs according to their characteristics such as period, velocity, and sometimes on the preferred direction of propagation. Large-scale TIDs usually have longer wavelengths (thousands of kilometers), periods exceeding an hour (in most cases), are to a large extent observed during geomagnetic disturbed conditions, and generally propagate equatorward from either hemisphere (e.g., Borries et al., 2009; Hajkowicz & Hunsucker, 1987; Hocke & Schlegel, 1996; Tsugawa et al., 2004; Valladares et al., 2009). Medium-scale TIDs can propagate in any direction and are launched by many processes including tropospheric systems and energy dissipation of large-scale TIDs.

In this study, we report on observations of large-scale traveling ionospheric disturbances (TIDs) during the most extreme space weather event (17 March 2015 storm) of solar cycle 24, focusing on the American, European-African, and Asian-Australian sectors. This particular storm period has received considerable attention and various ionospheric aspects related, but not limited, to global occurrence of equatorial plasma bubbles (Carter et al., 2016), ionospheric storm effects (e.g., Astafyeva et al., 2015; Fagundes et al., 2016; Nayak et al., 2016), and investigation of disturbance and direct penetration electric fields to low and equatorial latitudes (e.g., Kuai et al., 2016; Ramsingh et al., 2015) have already been presented in literature. With regard to large-scale TIDs, Zakharenkova et al. (2016) recently reported a global analysis of large-scale TIDs associated with the 17 March 2015 storm using a combination of GPS and GLONASS TEC data for the first time. The analysis in Zakharenkova et al. (2016) study concentrated on North American, European, and South American sectors and found series of TIDs with period ≈50–80 min and wavelengths 1,200–2,500 km. Borries et al. (2016) examined the properties of large-scale TIDs using Global Navigational Satellite Systems (GNSS)-derived TEC during the different phases of the 17 March 2015 storm over the European-African sector and reported three different types of wave-like structures with period and velocity values in the range of

1 – 2 h and 500 – 600 m/s. Both of these studies demonstrated that the equatorward large-scale TIDs originated from the auroral region during the storm main phase. Ramsingh et al. (2015) showed possible TID presence over the Indian sector during the recovery phase (on 18 March 2015).

Equatorward large-scale TIDs during geomagnetically disturbed conditions are usually linked to auroral region Joule-heating and Lorentz-coupling processes, and this has been well documented (e.g., Borries et al., 2009, 2016; Chimonas, 1969; Davis, 1971; Ding et al., 2007; Hines, 1960; Hajkowicz & Hunsucker, 1987; Hocke & Schlegel, 1996; Katamzi & Habarulema, 2014; Ngwira et al., 2012; Nicolls et al., 2004; Shiokawa et al., 2002, Tsugawa et al., 2003, 2004; Valladares et al., 2009; Zakharenkova et al., 2016). Theoretical and numerical modeling studies show that fluctuations in energy within the auroral regions due to storm-related processes significantly influence thermospheric composition thereby contributing to equatorward propagating large-scale TIDs (e.g., Balthazor & Moffett, 1997; Fuller-Rowell et al., 1994; Lu et al., 2001). Observations from different instrumentation such as ionosondes (e.g., Hajkowicz & Hunsucker, 1987; Prölss & Jung, 1978), incoherent scatter radars (e.g., Nicolls et al., 2004; van de Kamp et al., 2014), and GNSS (e.g., Borries et al., 2009, 2016; Katamzi & Habarulema, 2014; Ngwira et al., 2012; Nicolls et al., 2004; Shiokawa et al., 2002; Tsugawa et al., 2004; Zakharenkova et al., 2016, and some references therein) have all been used to determine the characteristics of large-scale TIDs. In this paper, we use a combination of GNSS, ionosonde, and SWARM data to study and report on new observations of large-scale TIDs propagating up to the topside ionosphere during the 17 March 2015 storm. Although equatorward large-scale TIDs for this storm period have already been reported (Borries et al., 2016; Zakharenkova et al., 2016), unique to this study are results of poleward TIDs over the American and African sectors originating from within the geomagnetic equatorial region. A detailed investigation has shown that poleward TIDs were launched during local daytime following a southward turning of the interplanetary magnetic field large-scale TID during the storm main phase. Analysis of $\mathbf{E} \times \mathbf{B}$ proxy data derived from equatorial and low-latitude magnetometer data showed increased vertical drifts over the American sector, highlighting the role of momentum transfer from ions and electrons to neutrals in launching poleward TIDs through Lorentz coupling (equatorial electrodynamics), a mechanism that was previously suggested by Knudsen (1969) and Chimonas (1969) but has not been comprehensively investigated with observations. Over the African sector, additional data are required to confirm the source of poleward TIDs. Using ionosonde electron density profile data, we also showed the vertical propagation of the equatorward large-scale TIDs. This provided the basis of a strong and direct observational evidence with regard to the role of TIDs in influencing altitudinal plasma distribution all the way to the topside ionosphere, which was observed through the enhancement of the SWARM in situ density data during periods when large-scale TIDs were present in GNSS data.

2. Data Sources and Methods

The 17 March 2015 storm was due to a coronal mass ejection (CME) that impacted the Earth's magnetosphere at ≈0445 UT as shown by the vertical red dashed line in Figure 1. The interplanetary and geomagnetic activity indices data for the 17 March 2015 storm have also been described in other sources (e.g., Astafyeva et al., 2015; Borries et al., 2016; Fagundes et al., 2016; Kuai et al., 2016; Nava et al., 2016; Ramsingh et al., 2015; Zakharenkova et al., 2016). Figure 1 shows variations in (a) solar wind velocity, Vsw (kilometers per second, km/s) (blue curve), B_z component of the interplanetary magnetic field, IMF B_z (nanoTeslas, nT) (black curve), (b) IMF B_x (blue curve) and IMF B_y (black curve) in nT, (c) *SYM-H* (nT) index (black curve), auroral electrojet, *AE* (nT) index (blue curve), and (d) the interplanetary electric field, IEF (millivolts per meter, mV/m). For the solar wind parameters, we have used the 1 min OMNI data (omniweb.gsfc.nasa.gov) propagated to the Earth's magnetosphere to coincide with the response observed from the geomagnetic field measurements. The *AE* and *SYM-H* indices were obtained from http://wdc.kugi.kyoto-u.ac.jp/wdc/Sec3.html. Figure 1a shows that during the storm sudden commencement (SSC), the solar wind velocity, Vsw increased from ≈400 km/s to 500 km/s, at the same time the IMF B_z turned northward and reached ≈26 nT at 0523 UT before shortly turning southward. Thereafter, B_z oscillated between north and southward directions until ≈1146 UT, when it remained southward (with exception of short duration northward turning at ≈1337 UT) for over 12 h. Immediately after the SSC (0447 nT), the values of B_x and B_y were ≈0 nT and 10 nT, respectively. During the recovery phase on 18 March 2015, B_x and B_y were largely positive and negative, respectively. Figure 1c shows that before the storm on 16 March 2015, the auroral region was relatively quiet and the *AE* index started gradually increasing after the SSC, and later reduced reaching minimum value at ≈1200 UT on 17 March 2015, and afterward, it immediately increased significantly during the main phase reaching a maximum value of 2,298 nT at 1358 UT.

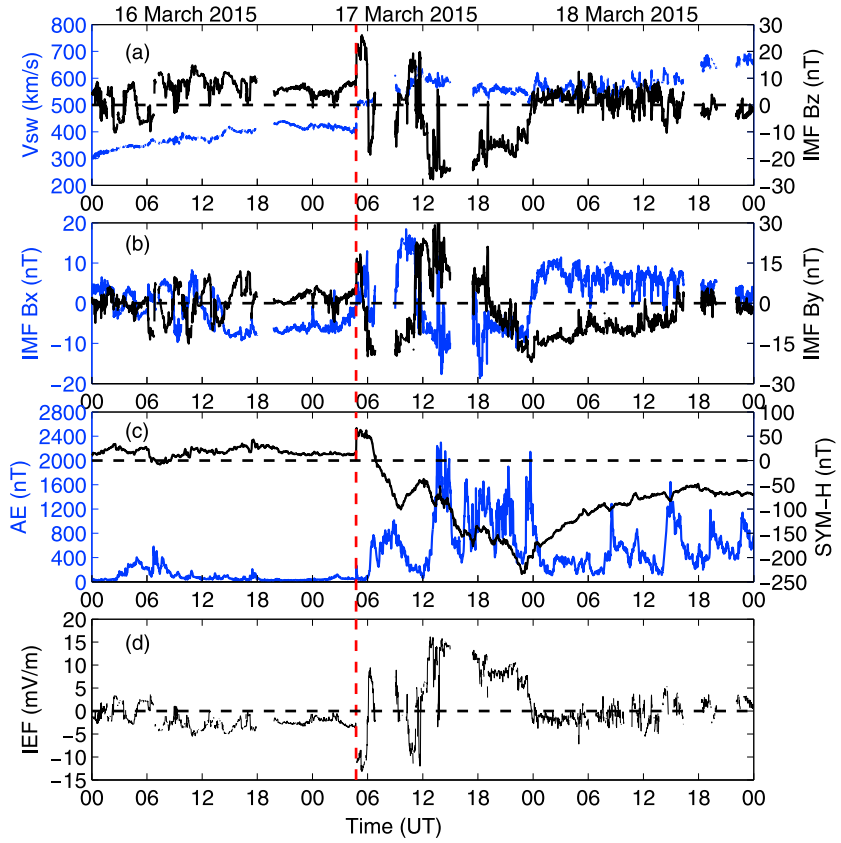

Figure 1. Variations of (a) solar wind velocity, Vsw (km/s), B_z component of the interplanetary magnetic field IMF B_z (nT), (b) IMF B_x and B_y, (c) symmetric component of the ring current, *SYM-H* (nT), and auroral electrojet, *AE* (nT) indices, and (d) interplanetary electric field, IEF (mV/m) for 16–18 March 2015. The red vertical dashed line represents shock time at 0445 UT on 17 March 2015. One minute solar wind data shifted to the Earth's magnetosphere were used.

Analysis of polar cap index has shown intense substorm activity during 17 March 2015 (e.g., Astafyeva et al., 2015; Borries et al., 2016). The *SYM-H* index experienced a pronounced minimum of −101 nT at 0937 UT before reaching a value of −234 nT at 2247 UT on 17 March 2015. Within about an hour of the storm recovery phase, the *AE* index reached another maximum value of 2,145 nT (at 2342 UT) on 17 March 2015. The IEF varied between −5 mV/m and 5 mV/m before the storm and reached ≈ −13 mV/m (0523 UT) soon after the SSC. About 13 h after the commencement of the main phase, the IEF value reached its maximum (≈16 mV/m at 1248 nT).

2.1. TEC Data

We have processed GNSS RINEX data from over 2,700 receiver stations for the 17 March 2015 to derive TEC at 30 s time resolution. To estimate the background TEC during the 17 March 2015 storm, a fourth-order fit to the slant TEC segment from each satellite that is visible over a particular receiver location has been used. A direct subtraction of fitted TEC from derived TEC yielded TEC residuals (ΔTEC) which show the level of disturbance induced in TEC due to forcing either from below, above, or both. This procedure was repeated for all TEC segments from all stations considered (about 2,700) for 17 March 2015. A similar method has been used in TID-related studies (e.g., Ding et al., 2007; Habarulema et al., 2016; Valladares et al., 2009). To minimize multipath-related fluctuations, a 20° elevation cutoff was considered. ΔTEC at ionospheric pierce points (IPPs) at altitude of 350 km was then binned within 3 min × 0.8° (time/latitude) to identify the presence of large-scale TIDs. To observe large-scale TIDs, diurnal ΔTEC maps with respect to selected latitude ranges were generated within similar longitude sector spanning 40°. Latitudinal coverage of 50°S–50°N, 40°S–60°N, and 40°S–45°N were chosen (mainly based on data availability) for the American, African, and Asian sectors, respectively. Figure 2 shows (a) the distribution of GNSS receiver locations used to derive TEC data, and (b) the typical spatial data coverage shown by ΔTEC variability (considered at IPPs) binned within 2.5° × 4°

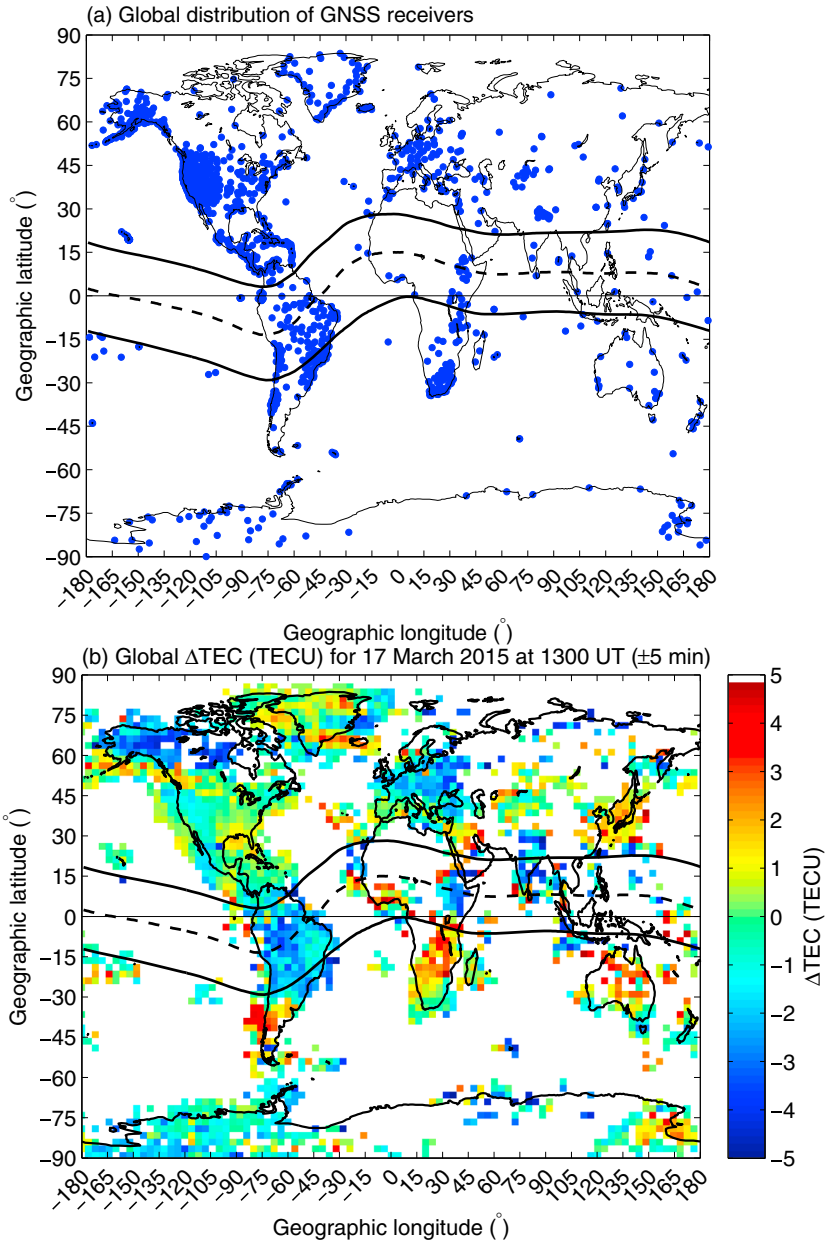

Figure 2. (a) Global distribution of GNSS receiver locations and (b) typical spatial coverage of ΔTEC (TECU) variability (considered at IPPs) binned within 2.5° × 4° (latitude/longitude) at 1,300 UT (±5 min).

(latitude/longitude) at 1300 UT (±5 min). Although we mentioned that we have used 40° longitude span, in most cases, the coverage is limited by the GNSS sensor network distribution. For example, for the African sector, Southern Hemisphere, the land mass that has data coverage is mostly from 15°E–40°E translating into a longitude coverage of 25° that was used by Figueiredo et al. (2017). Similarly, for the South American Southern Hemisphere, data coverage is roughly from 50°W–75°W for latitudes 60°S–30°S.

2.2. Geomagnetic and E × B Drift Data

The use of horizontal component of the Earth's magnetic field from magnetometer data through the differential magnetometer approach (Rastogi & Klobuchar, 1990) is well established as a basis for estimating ionospheric **E** × **B** drift from the determination of the equatorial electrojet (EEJ) (Anderson et al., 2002; Yizengaw et al., 2011, 2012, 2014). Because the EEJ is stronger during the dayside and almost zero at night, the method of estimating vertical drift from magnetometer observations is reliable only during local daytime. This approach uses a magnetometer station located at the equator and another one away from the equator

Table 1
Magnetometer Stations Used to Estimate EEJ Over the American, African, and Asian Sectors in This Study

			Geographic coordinates		Geomagnetic coordinates	
Station	Code	Network	Latitude	Longitude	Latitude	Longitude
		American sector				
Alta Floresta	ALT	LISN	−9.9	−56.1	0.8	15.2
Cuiba	CUB	LISN	−15.6	−56.1	5.9	13.8
		African sector				
Addis Ababa	AAE	INTERMAGNET	9.0	38.8	0.2	110.5
		Asian sector				
Phuket	PUKT	AMBER	7.9	98.4	−0.6	170.0
Bangkok	BAGK	AMBER	14.08	100.61	6.2	172.2

by 6° – 9° (Anderson et al., 2002; Yizengaw et al., 2011). Further, detailed information about drift estimation from magnetometer data can be found in Anderson et al. (2002), Yizengaw et al. (2011, 2012), and Yamazaki and Maute (2016). Table 1 shows pairs of magnetometer stations (along with their geographic and geomagnetic locations) used in the estimation of EEJ on 17 March 2015 for the American, African, and Asian sectors. These magnetometer stations belong to Low-Latitude Ionospheric Sensor Network (LISN) project (Valladares & Chau, 2012), International Magnetic Network (INTERMAGNET), and African Meridian and B-Field Education Research (AMBER) project (Yizengaw & Moldwin, 2009) networks for the American, African, and Asian sectors, respectively. For the African sector, we used only single station to estimate the EEJ due to data unavailability for the second station during the 17 March 2015 storm. For the American sector, we have made use of the 150 km drift echoes from Jicarmaca Unattended Long-Term studies of the Ionosphere and Atmosphere (JULIA) system, which have been shown to approximate the F_2 region vertical drifts well (Chau & Woodman, 2004; Yizengaw et al., 2011, 2014), and with C/NOFS for the African sector (Yizengaw et al., 2011).

3. Results

Figure 3 shows ΔTEC (TECU), ΔH (nT) (a proxy of $\mathbf{E} \times \mathbf{B}$ drift), and SWARM-B in situ density (*Ne*) over the American, African, and Asian sectors for the 17 March 2015. Figures 3a, 3c, and 3e shows the latitude/time ΔTEC maps over American, African, and Asian sectors within a longitude sector of 40°. Although we have considered a wide longitude range, our results are in excellent agreement with the study of Zakharenkova et al. (2016) in their Figures 4b and 3d for the European (10°E ± 5°) and South American (65°W ± 5°) sectors, respectively, in the identification of equatorward large-scale TIDs. Only ΔTEC magnitudes differ due to the different methods used in estimating the background TEC values. Figures 3b and 3f show Δ*H* over Alta Floresta, ALT (0.8°N, geomagnetic) in the American sector, and Phuket, PUKT (0.6°N, geomagnetic) for the Asian sector, representing dynamics of EEJ which is a proxy of vertical drifts over the respective equatorial regions. For the African sector, there were no data for the second magnetometer station to derive Δ*H* in a similar way as the other sectors. Thus, we used a single station (located at the geomagnetic equator, 0.2°N) to estimate the EEJ in the African sector on 17 March 2015. In order to do this, we have applied the following procedure to the *H* component field observed at the geomagnetic equator. First, daily magnetic field variation is identified by subtracting the monthly averaged background geomagnetic field value, which is also approximately equal to the secular field level. This procedure also removes secular field values from the daily *H* component field. The background geomagnetic field is calculated by taking the nightside (2200 – 0200 LT) average of the quiet days ($Kp < 2$) magnetic field readings of a given month. The next step is removing magnetic variations associated to Sq and ring current contributions. This can be accomplished by including data from quiet days of the month ($Kp < 2$) and determining an average value for every 30 min interval. The 48 distinct values are then interpolated to a time resolution of 1 min, and subtracted from the daily data within the given month. This procedure also removes the magnetic field variation associated to the solar diurnal tide. The ring current contribution to the magnetic field disturbance is also removed by subtracting the *Dst* index. We used 1 min resolution *SYM-H* index. Finally, a significant factor that we removed is the noncyclic change. The noncyclic changes, which may be the result of slow magnetospheric recovery on quiet days from earlier geomagnetic disturbances, are generally negligibly small since the *Dst* is already removed. It is defined as the difference between the beginning and end values of the day (Matsushita & Campbell, 1972). The noncyclic

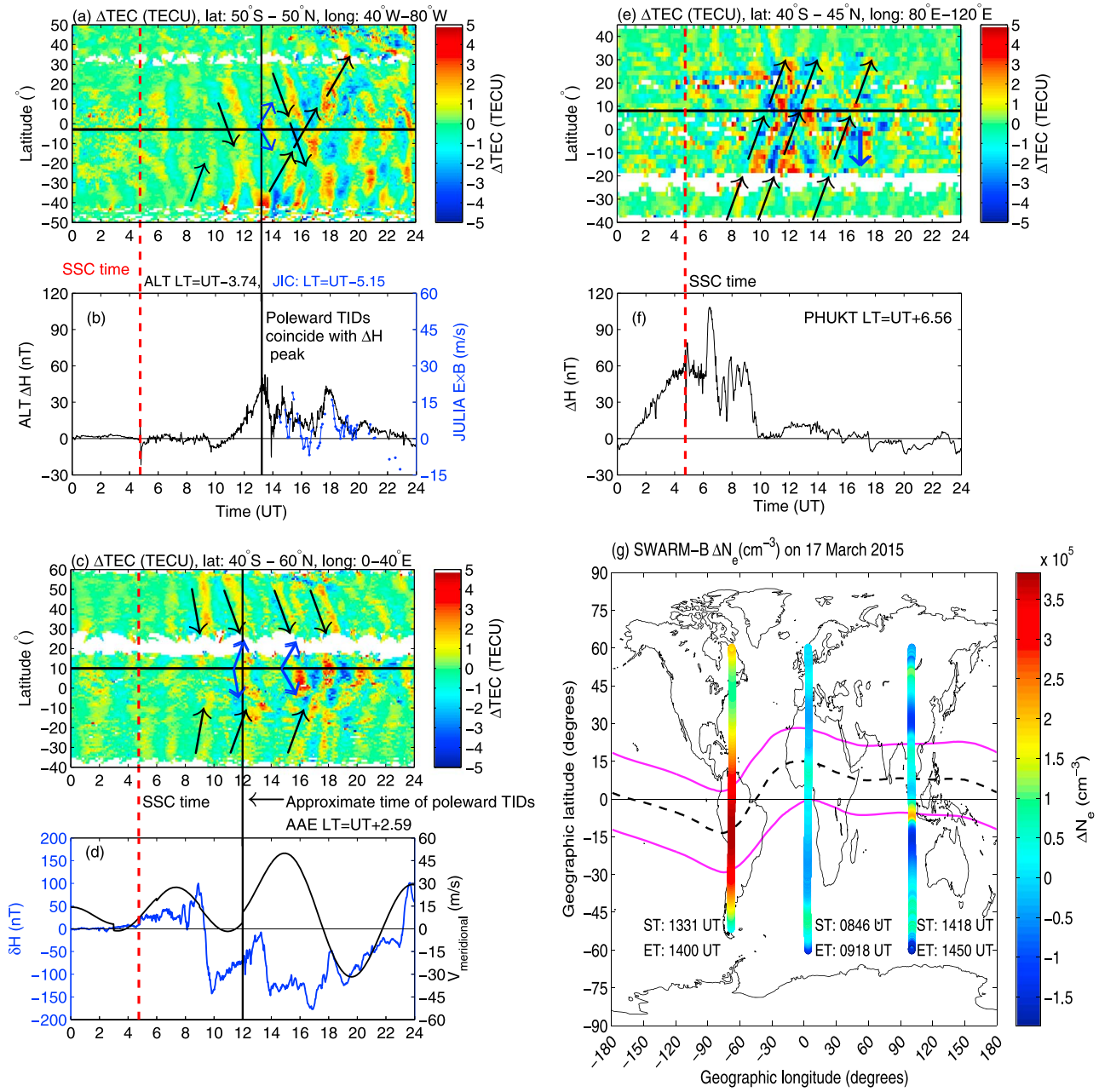

Figure 3. Variations of (a) American sector ΔTEC (TECU) and (b) ΔH (nT) and JULIA **E** × **B**; (c) African sector ΔTEC (TECU) and (d) δH (nT) and meridional wind velocity (m/s) from HWM; (e) Asian sector ΔTEC , (f) ΔH (nT), and (g) SWARM-B electron density on 17 March 2015. The solid lines in Figures 3a, 3c, and 3e approximate the geomagnetic equator in the three sectors. Vertical black lines in Figures 3a–3d show approximate times when poleward TIDs were observed over the American and African sectors.

change value is then subtracted from the residual on a daily basis. After removing all the contributions mentioned above, the residual magnetic variations is mainly due to EEJ current, which is plotted as a function of time as shown in Figure 3d (blue curve). The black curve in Figure 3d shows the meridional wind velocity from the Horizontal Wind Model (HWM) over AAE on 17 March 2015. For the American sector, **E** × **B** drift values from JULIA (blue curve) are also shown in Figure 3b. The red dashed line in Figure 2 shows the SSC time for the geomagnetic storm at 0445 UT. The American sector displays mostly equatorward TIDs from both hemispheres crossing over to either hemisphere as indicated by black arrows in Figure 3a. There appears to be a case of poleward TIDs with geomagnetic equatorial origin just after 1300 UT as shown by the blue arrows and black straight line in Figures 3a and 3b. For the African sector (Figure 3c), poleward TIDs are clearly identified at

around 1200 UT (approximate time is shown by the vertical black line) and 1500 UT. The blue arrows indicate the apparent direction of poleward TIDs. For the 1500 UT observation, the northward propagation is not clear due to lack of observational data. In Figure 3c, equatorward TIDs appear at around ≈0900 UT, 1200 UT, 1600 UT, and 1800 UT from both Northern and Southern Hemispheres. We note that δH (in Figure 3d) is substantially reduced during the observation of poleward TIDs in the African sector. Nevertheless, in absence of the second set of magnetometer observations, we observe that the direction of the electric field was westward during epochs of poleward TIDs appearances. Although the data are noisy, the Asian sector shows equatorward TIDs from the Southern to the Northern Hemisphere as seen in Figure 3e. One case at ≈1700 UT appears to show poleward TIDs (for the Southern Hemisphere), but there is no corresponding similar observation on the Northern Hemisphere to conclude about its origin. A common observation in all the three sectors is the existence of secondary waves that seem to propagate along the identified TID signatures crossing the equator. These secondary waves exhibit low ΔTEC values which translate into low amplitudes and have been previously observed (e.g., Hajkowicz & Hunsucker, 1987; Thome, 1968) and also shown through theoretical/numerical simulations (e.g., Balthazor & Moffett, 1997) following storm/substorm activities. Figure 3g shows changes in SWARM-B N_e (ΔN_e) over the American sector (67.6°W), African sector (3.8°E), and Asian sector (100.5°E). ΔN_e (cm^{-3}) is obtained by fitting a fourth-order polynomial to SWARM N_e data and subtracting fitted from actual N_e values in the three sectors. SWARM satellites provide local density measurements using onboard Langmuir probes (Buchert et al., 2015). Over the American sector, the depletion in SWARM-B N_e after 45°S is also well seen in the ΔTEC results at ≈1,400 UT. We observe increased N_e toward high-latitude regions during similar times in the presence of large-scale TIDs especially for the African-European and Asian sectors. This points to the evidence of TIDs' propagation all the way to the topside ionosphere as we will show in the next section using ionosonde data over the African sector in the Southern Hemisphere.

4. Discussion

In our analysis, all three sectors show equatorward TIDs and are more clear for the American and African sectors. Similar/related results have been reported elsewhere (e.g., Borries et al., 2016; Zakharenkova et al., 2016). A new observation is the existence of large-scale TIDs which appear to have originated from the geomagnetic equator in both American and African sectors. Figures 4a and 4b show extracts of ΔTEC at geographic latitudes 5°S, 10°S, and 15°S in the Southern Hemisphere and 0°, 5°N, and 10°N for the Northern Hemisphere within the American sector during 1230 UT – 1500 UT when poleward TIDs are observed. Here we recall that the geomagnetic equator has been approximated at geographic latitude 3.5°S in Figure 3a. Figures 4c and 4d shows results obtained by cross correlating ΔTEC time series at different latitudes in Figures 4a and 4b. For example, in Figure 4c, the cross correlation was performed between ΔTEC time series at latitudes 5°S and 10°S (shown in blue color as 5°S – 10°S) and 10°S – 15°S (red curve). The cross-correlation method (CCM) provides the time lag when the two ΔTEC time series at the considered latitudes are highly correlated/similar. Based on time lags determined using the CCM between ΔTEC series variability at different latitudes, the estimated velocity values of the large-scale TIDs are 688 ± 84 m/s and 686 ± 120 m/s in the Southern and Northern Hemispheres (Figures 4c and 4d), respectively. Within the African sector, the geomagnetic equator is estimated at 10°N and Figures 4e and 4f show ΔTEC changes at geographic latitudes 5°N, 3°S, 10°S and 10°N, and 15°N for the Southern and Northern Hemispheres wave propagation, respectively. Figure 4g shows the cross-correlation results for the African sector Southern Hemisphere with velocity of about 422 ± 126 m/s between 1100 UT and 1400 UT. Due to lack of data within the Northern Hemisphere in the African sector, we have estimated the velocity of poleward TIDs based on two latitudes 10°N and 15°N (Figure 4h). The estimated velocity is 539 ± 80 m/s, which is statistically comparable with the Southern Hemisphere determined value. While equatorward TIDs are known to be launched from the auroral regions during storms (e.g., Davis, 1971; Georges & Hooke, 1970; Prölss & Jung, 1978; Valladares et al., 2009), results about poleward TIDs of geomagnetic equator origin are relatively new and physical mechanisms for their launching are not fully understood. Long-term statistical studies about when and how often they occur are still unavailable. Observations of large-scale TIDs over China during the storm recovery phase were attributed to the excitation arising from medium-scale disturbances (Ding et al., 2013). Possibility of EEJ generating waves similar to TIDs was put forward by Knudsen (1969), and variations of $\mathbf{E} \times \mathbf{B}$ drifts were suggested to be responsible for their launching through Lorentz coupling of the lower ionospheric layer to the neutral atmosphere during daytime (Chimonas, 1969). Recently, clear correlation between daytime $\mathbf{E} \times \mathbf{B}$ variability and occurrence of poleward TIDs was reported for the African and American sectors (Habarulema et al., 2015, 2016). However, their probable causes are not clear

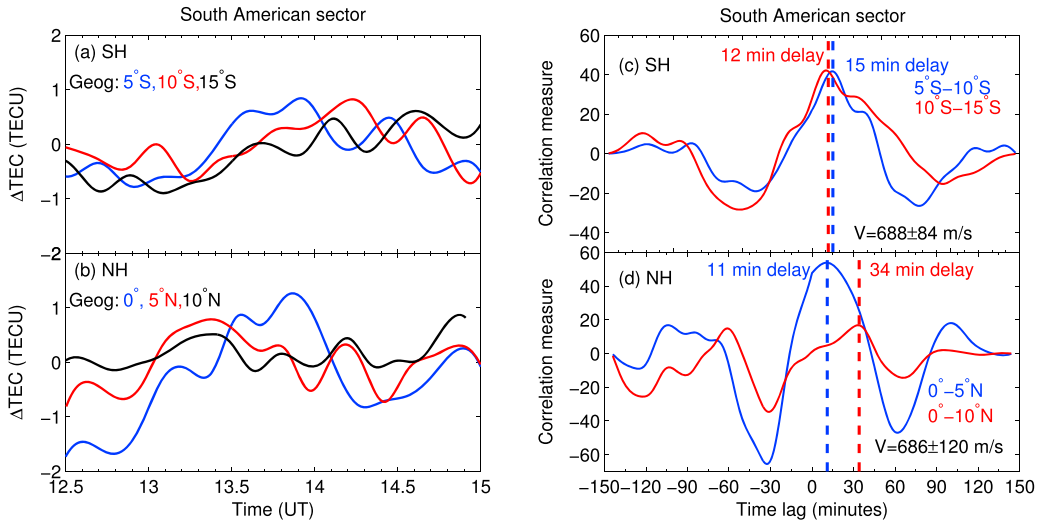

ΔTEC (TECU) at (a) 5°S, 10°S, and 15°S; (b) 0°, 5°N and 10°N; and the TIDs' estimated velocity values using the cross correlation method ((c) and (d)) in the SH and NH respectively over the American sector

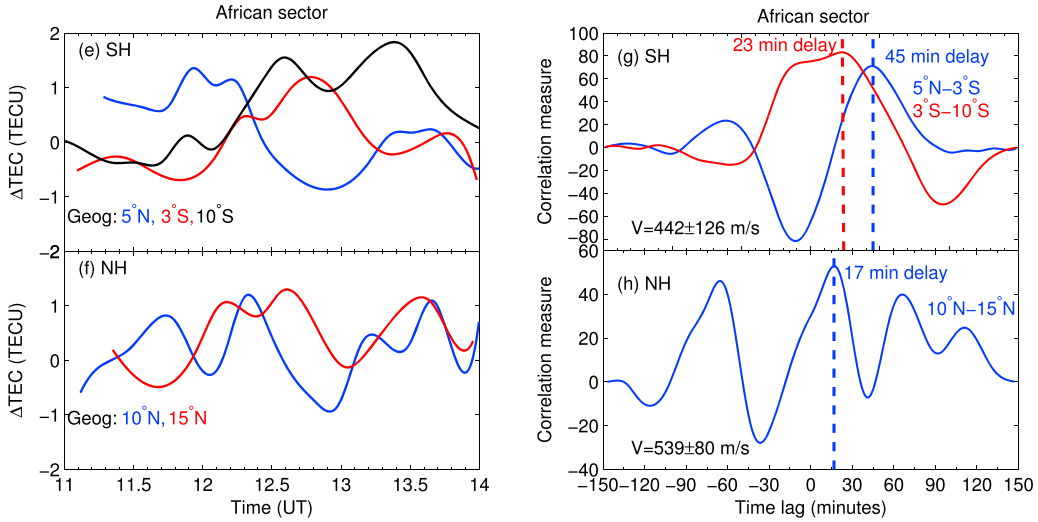

ΔTEC (TECU) at (e) 5°N, 3°S, and 10°S; (f) 10°N and 15°N; and the TIDs' estimated velocity values using the cross correlation method ((g) and (h)) in the SH and NH respectively over the African sector

Figure 4. Extracted ΔTEC (TECU) at different geographic latitudes within the same longitude sector to compute velocity values of poleward TIDs in the American sector for the (a) Southern Hemisphere (SH) and (b) Northern Hemisphere (NH) between 1230 and 1500 UT. (c, d) The cross-correlation results for the estimated velocities. ΔTEC (TECU) variations for selected latitudes over the African sector are shown in (e) SH and (f) NH during 1100–1400 UT with the (g, h) the corresponding determined velocity values. In Figures 4c, 4d, 4g, and 4h, vertical dashed blue and red lines show the time lags at which ΔTEC time series data at two latitudes are highly correlated.

during the nighttime. To understand the likely cause of poleward TIDs originating from the geomagnetic equator, we examine the behavior of IMF B_z and the response of the $\mathbf{E} \times \mathbf{B}$ (ΔH) during the presence of poleward TID observations. In Figure 1a, B_z turned southward at ≈1,150 UT until 1336 UT. Within this duration, we observed poleward TIDs in the American sector, which coincided well with the peaking of ΔH at ≈1314 UT over ALT (0.8°N, geomagnetic) as shown in Figures 3a and 3b. JULIA $\mathbf{E} \times \mathbf{B}$ data (Figure 3b) are in agreement with ΔH during periods when they are all available. Increased ΔH ($\mathbf{E} \times \mathbf{B}$) were caused by penetration electric fields starting at ≈1200 UT in the American sector (Kuai et al., 2016) as a result of the increase in IEF (Figure 1d) during the southward turning of the IMF (Figure 1a). Penetration electric fields are eastward (westward) during the local daytime (nighttime) (e.g., Fejer & Scherliess, 1998; Huang et al., 2005). Daytime-penetrating electric

field enhances the existing eastward electric field, and thus vertical drift in low/equatorial latitudes leading to force and momentum transfer from the ionized particles to neutrals (through Lorentz coupling), giving rise to atmospheric gravity waves, and hence possibly contributing to the observed TIDs (Chimonas, 1969; Habarulema et al., 2016; Knudsen, 1969). We therefore conclude that low-latitude electrodynamics linked to increased $\mathbf{E} \times \mathbf{B}$ as a result of prompt penetration electric fields were responsible for launching poleward TIDs (from the geomagnetic equator) observed over the American sector during 1230–1500 UT. For the African sector, we see that during launching of poleward TIDs (≈1200 UT, see Figures 3c and 3d), δH variations show westward electric field at equatorial latitudes. At around 0900 UT, we observe a sharp reduction in δH for about an hour (Figure 3d). A reduction in EEJ corresponds to existence of westward electric fields and hence decrease in $\mathbf{E} \times \mathbf{B}$, which can be due to the disturbed dynamo mechanism during local daytime in equatorial ionosphere (e.g., Blanc & Richmond, 1980). We also note that after ~0615 UT, the IMF B_z turned northward and alternated between northward and southward directions until ~1150 UT on 17 March 2015. When IMF B_z abruptly turns northward, the dayside low/equatorial latitude ionosphere exhibits westward electric fields as a result of overshielding (e.g., Kelley et al., 1979). Both overshielding and disturbed dynamo electric fields reduce the EEJ and thus $\mathbf{E} \times \mathbf{B}$ drift. Due to this, increased $\mathbf{E} \times \mathbf{B}$ may therefore not be responsible for the observed poleward TIDs (1100–1400 UT) over the African sector on 17 March 2015. We, however, note that increased TEC starting at around 1115 UT has been reported over the African sector (Borries et al., 2016; Nava et al., 2016) and penetrating electric fields were present during the southward turning of IMF large-scale TID (Nava et al., 2016) alongside disturbed dynamo electric field. Figure 3d shows meridional wind velocity (black curve) from the Horizontal Wind Model, HWM (Drob et al., 2008) over the same location (AAE) at altitude of 350 km for 17 March 2015. We note that there was a sudden jump from ≈4 m/s to 11 m/s at 1200 UT, and thereafter, the meridional wind velocity continued increasing. Given its direction, it is feasible to suggest that meridional wind velocity could have played a role in propagation of poleward TIDs in the Northern Hemisphere, but it is still not clear what was responsible for the Southern Hemisphere observations. This aspect requires more direct meridional wind data and hence further investigation. The physical mechanism for launching the observed poleward TIDs also requires further work.

Despite the increased $\mathbf{E} \times \mathbf{B}$ drift over the Asian sector (Figure 3f), we have not observed clear poleward TIDs originating from the geomagnetic equator. There is an isolated case at around 1700 UT in the Southern Hemisphere, with no clear reference of having originated from the equatorial region. Data over this sector were also sparse compared to other sectors. Nevertheless, there are clear examples of equatorward TIDs crossing over to the Northern Hemisphere as shown in Figure 3e. Figure 5 shows examples of TID signatures demonstrating waves propagating and crossing over to either hemisphere over the American (1030-1230 UT) and Asian (0900-1200 UT) sectors. Figures 5a and 5b shows ΔTEC at latitudes 15°N, 0°, and 15°S; and the corresponding velocity estimation from the CCM as 1241 ± 252 m/s (1030–1230 UT) for the north-south propagation. For the same storm period, Borries et al. (2016) reported the large-scale TID between 60°N–31°N over the European region with velocity 1100 ± 200 m/s, which statistically agrees with our determined value for the American sector. Figure 5c presents ΔTEC variability at latitudes 10°S, 5°S, and 10°N over the Asian sector (0900–1200 UT). The corresponding computed velocity is 846 ± 125 m/s (Figure 5d). Figures 5a and 5c are directly extracted from data used to generate Figures 3a and 3e at the respective times considered. While this equatorward propagation analysis was done at different times, we observe that the velocity values differ perhaps due to the amount of ΔTEC data used in both sectors. In this context, there was less data available for the Asian sector compared to the American sector in the computation of the TIDs' velocities. However, the calculated velocities for both sectors are within the range of values for equatorward large-scale TIDs. We note that previous studies of this storm left out the Asian-Australian sector analysis (e.g., Zakharenkova et al., 2016) due to limited data coverage to conduct a detailed investigation. For the American sector (Figure 3a), there is an interesting feature of two TIDs propagating from Southern and Northern Hemispheres, crossing the geomagnetic equator and interfering at ≈10°S–20°S, geographic between ≈1500 and 1830 UT. Both TIDs continue to either hemisphere. The TID originating from the Southern Hemisphere had a velocity of ≈638 m/s. After interfering with its Northern Hemisphere counterpart, it continued to propagate in the Northern Hemisphere with a phase velocity of ≈649 m/s. This is consistent with theoretical and observational studies that large-scale TIDs of auroral origin interfere and continue to propagate to either hemisphere with unchanged velocity (e.g., Balthazor & Moffett, 1997; Pradipita et al., 2016). For the American sector, typical velocities reported

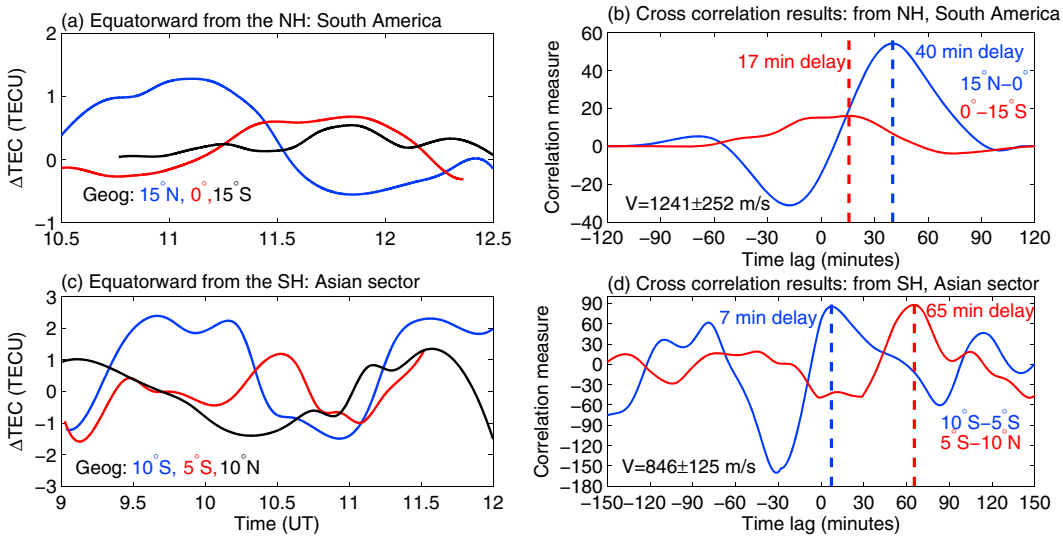

Figure 5. An example showing velocities for equatorward propagating TIDs for the (a) American sector (1030–1230 UT) from the NH and the determined velocities (b) based on the CCM method; and (c) Asian sector (0900–1100 UT) from the SH on 17 March 2015 with (d) velocity results.

previously for the equatorward TIDs during storms were 700 m/s (Valladares et al., 2009) for the 29–30 October 2003 storm, 600 m/s for the 1–2 October storm (Nicolls et al., 2004), and more recently 700 m/s for the 26 September 2011 storm (Pradipita et al., 2016). Over Europe, Borries et al. (2009) reported velocities in range of ≈300–1100 m/s in their extensive analysis of storm-induced TIDs during storms of 2001–2007.

An intriguing result has been the observation of increased in situ N_e from SWARM toward high latitudes during periods when TIDs are present in GNSS TEC data. Also, the SWARM TEC data (https://vires.services/) confirm the increased latitudinal profile of the topside N_e. For example, as seen in Figure 3g, SWARM-B N_e showed an increase over the African-European sector (e.g., ≈45°S–55°S for the Southern Hemisphere) during similar time (0800–0900 UT) when equatorward large-scale TIDs are observed. A similar result is visible over the north African-European sector. Figure 6 shows this more clearly where SWARM-B displays enhanced N_e in both hemispheres over the African-European sector on 17 March 2015. To approximate the N_e deviation on a storm day from the normal variability, we fitted a fourth-order polynomial to SWARM-B N_e data over the African-European sector and computed the difference between actual and fitted N_e values to obtain ΔN_e. We then calculate the ratio of ΔN_e to N_e ($\Delta N_e/N_e$) to obtain scale-free ionospheric N_e variability at different latitudes. Figure 6 shows $\Delta N_e/N_e$ from SWARM-B as a function of geographic latitude and time (0846–0918 UT) along ≈4°E longitude. An increase in N_e is observed in SWARM-B N_e data as shown by the cyan blocks, which are equidistant from the geographic equator. The magenta block indicates the N_e enhancement over the low latitudes. We notice that the N_e increase was greater in the Southern Hemisphere. The storm-induced equatorward winds are in the same direction as the background thermospheric neutral winds (which usually blow from the summer to winter hemisphere) in the Southern Hemisphere. In addition to the equatorward TIDs, these will move N_e to higher altitudes, which is the likely reason of greater N_e enhancement in the south compared to Northern Hemisphere. In the Northern Hemisphere, storm-induced winds and equatorward TIDs are in opposite direction as the background thermospheric neutral winds in March equinox (which is close to winter). During the time interval of SWARM-B data availability, signatures of large-scale TIDs are evident in Figure 3c in both hemispheres. It is known that TIDs can move *F* region plasma to high altitudes where the loss rate is lower, contributing to positive storm effects through the enhancement of ionospheric N_e (e.g., Ding et al., 2007; Hajkowicz & Hunsucker, 1987;

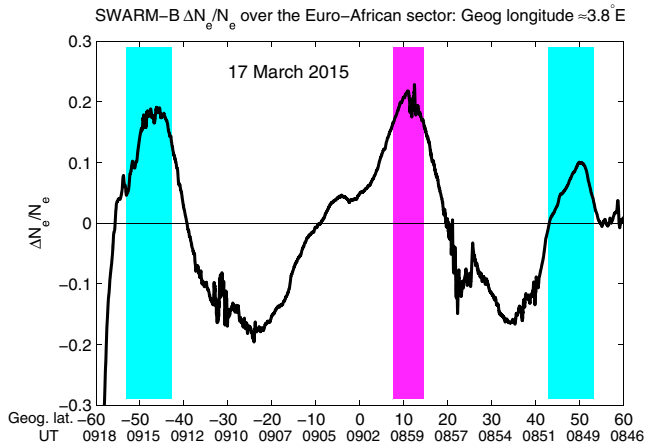

Figure 6. Changes in SWARM-B N_e changes on 17 March 2015 over the European-African sector during 0846–0918 UT. Enhanced N_e in the Southern and Northern Hemispheres are higlighted by the cyan blocks. The magenta block shows increased N_e over low latitudes around the geomagnetic equator.

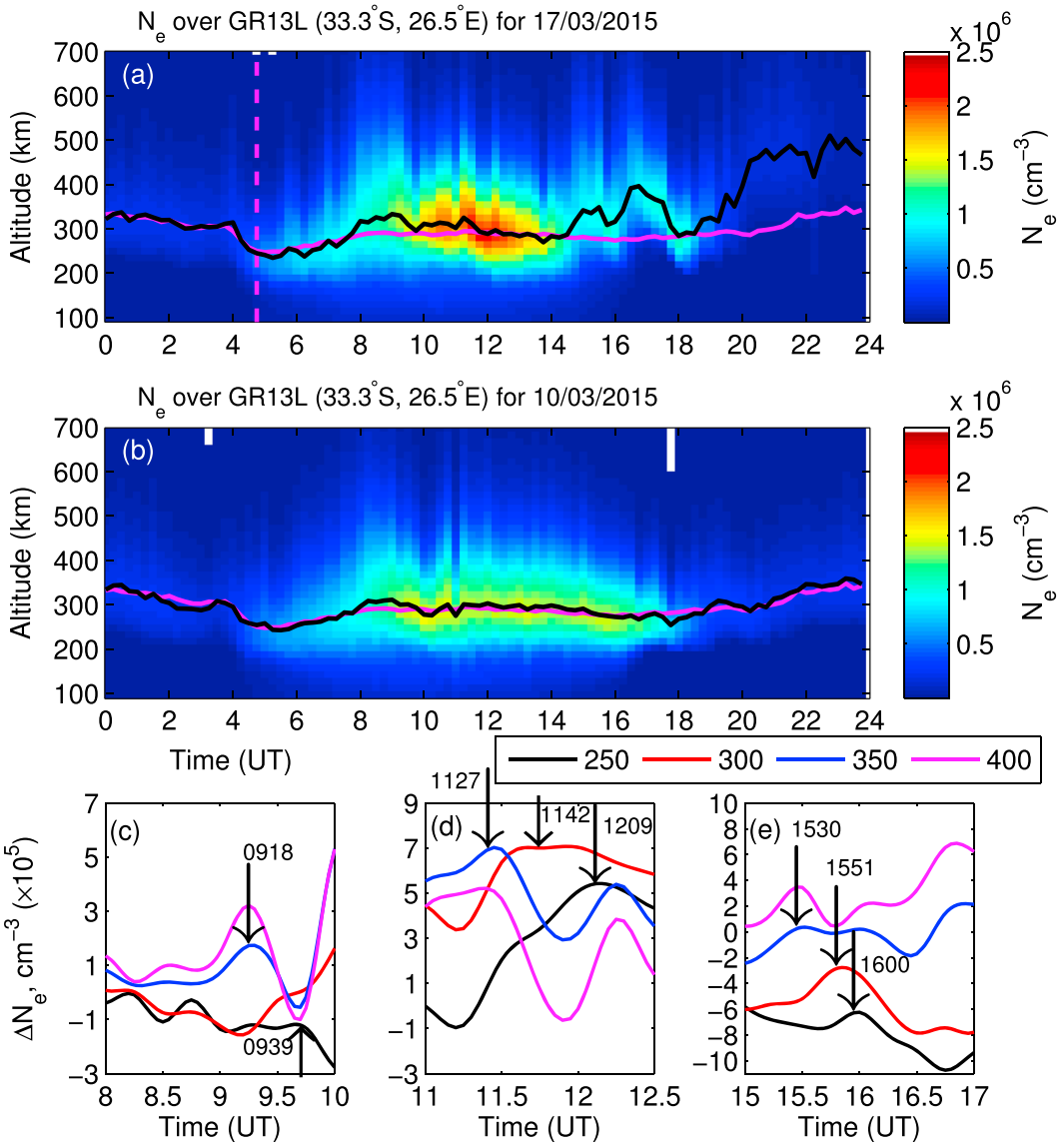

Figure 7. Ionosonde N_e variations over GR13L for (a) 17 March and (b) 10 March 2015. The solid black and magenta lines show h_mF_2 (on 17 and 10 March 2015) and monthly median h_mF_2 values, respectively. (c–e) Zoomed in details of ΔN_e computed by subtracting extracted N_e data on 10 March from 17 March 2015 values at altitudes 250 km (black curve), 300 km (red curve), 350 km (blue), and 400 km (magenta) during periods (0800–1000 UT, 1100–1230 UT, and 1500–1700 UT) when TIDs are observed in GPS data. Times of peak occurrences at different altitudes are shown in each panel with black arrows.

Ngwira et al., 2012; Prölss & Jung, 1978; Tsugawa et al., 2004). To further investigate whether large-scale TIDs contributed to enhanced N_e in SWARM data, Figures 7a and 7b show altitudinal variation of N_e over the ionosonde station Grahamstown, GR13L (33.3°S, 26.5°E), South Africa, for 17 and 10 March 2015. The 10 March 2015 was the most quiet day of the month and its values serve as the background N_e variability. The altitude and time ranges used for binning N_e are 15 km and 15 min, respectively. The solid magenta line represents monthly median h_mF_2 variability while the black solid line is a plot of h_mF_2 values for 17 and 10 March 2015. Careful ionosonde data checking was done and storm time ionograms edited where it was found necessary. The real heights are derived from virtual heights using a technique described in Reinisch and Hunag (1983) and Huang and Reinisch (1996). A previous study investigating ionospheric storm effects during the 17 March 2015 reported positive storm effect over South African midlatitudes using ionosonde data including information over GR13L (Nayak et al., 2016). In this paper, our usage of GR13L data is aimed at studying the vertical propagation of large-scale TIDs toward the topside ionosphere and is therefore completely different from

results presented in Nayak et al. (2016). We recall that during periods when equatorward TIDs are seen in GNSS data over Southern Hemisphere, there is a significant enhancement of N_e toward high altitudes (Figure 3g over the European-African sector) and Figure 7a shows that h_mF_2 was elevated above the background monthly median values especially between ≈0800–0930 UT and 1500–1800 UT. To observe N_e changes at different altitudes, we extracted N_e values at 250 km, 300 km, 350 km, and 400 km from Figures 7a–7b, and performed a cubic spline interpolation at a resolution of 3 min for each altitude's N_e. Original ionosonde data had a time resolution of 15 min. Quiet time N_e data (10 March 2015) were then subtracted from corresponding disturbed time values (17 March 2015) to obtain ΔN_e plotted in Figures 7c–7e during periods (0800–1000 UT, 1100–1230 UT, and 1500–1700 UT) when meridional propagation of TIDs is clearly visible in GNSS data (Figure 3c). In all cases, it is observed that peak occurrences appear first at 400 km and last at 250 km altitude. In Figures 7c–7e, the peak at 400 km always appeared 3 min before the N_e peak at 350 km. Because the ionosonde measures the bottomside ionosphere up to the h_mF_2 peak (∼350 km), we excluded extrapolation results at 400 km in our phase velocity estimations. Figure 7c indicates peaks in N_e values at 0918 UT and 0939 UT for 350 km and 250 km, respectively. No clear maximum N_e value was identified at 300 km. These results reveal a downward phase propagation with velocity of ∼80 m/s. Similarly, peak occurrences at 1127 UT, 1142 UT, and 1209 UT (for 350 km, 300 km, and 250 km) give downward phase velocity of ≈43 ± 16 m/s in Figure 7d. In Figure 7e, the N_e peak at 350 km occurred at 1530 UT, while altitudes 300 km and 250 km show peaks at 1551 UT and 1600 UT, respectively, giving estimated velocity of 66 ± 37 m/s. The calculated vertical wavelength is in the range ≈54–100 km. Downward phase velocities for TIDs is a well-known theoretical property (e.g., Hines, 1960; van Velthoven, 1990) due to the propagation of phase and energy in opposite vertical directions within the atmosphere. While the ionosonde data time resolution may be too low to accurately determine the TIDs' vertical characteristics, it is remarkable that for all the instances when meridional propagation of TIDs was observed in GNSS data, ionosonde data showed downward phase TID propagation which is consistent with other studies that have used incoherent scatter radar data (e.g., Nicolls et al., 2004; van de Kamp et al., 2014). A combination of ionosonde results and in situ N_e data from SWARM-B (which is at altitude of 520 km) gives us confidence to suggest that resulting TIDs from the launched gravity waves can reach the topside ionosphere. This is the first time that such result has been seen (based on ionosonde data over the African sector) showing a clear link of TIDs influencing altitudinal plasma distribution from bottomside to topside ionosphere.

5. Conclusions

Similar to existing studies during the 17 March 2015 storm period (Borries et al., 2016; Zakharenkova et al., 2016), we have reported the presence of large-scale TIDs over the American, European-African, and Asian-Australian sectors. Large-scale TIDs propagated and crossed over to either hemisphere in American and Asian sectors, although the latter had a limited data set for comprehensive investigations to be undertaken. Over the African-European sector, lack of data in the Northern Hemisphere over the African region hindered us from establishing whether the TID from the European region reached the equator. We have shown that poleward TIDs were launched from the geomagnetic equatorial region (over the African sector just before 1200 UT) and propagated with velocities of ≈440 m/s and 540 m/s in the Southern and Northern Hemispheres, respectively. The driving mechanism for poleward TIDs observations over this region on 17 March 2015 has not been established. Over the American sector, poleward TIDs propagated with ≈690 m/s in Southern and Northern Hemispheres. In the American sector, poleward TIDs were launched by low-latitude electrodynamics as a result of enhanced eastward electric field due to penetrating electric field during the southward turning of IMF B_z. Enhanced eastward electric field led to increased vertical $\mathbf{E} \times \mathbf{B}$ that made Lorentz coupling effective in launching poleward TIDs through the energy transfer from ionized particles to neutrals (Knudsen, 1969; Chimonas, 1969). Equatorward TIDs have been observed to cross over from either hemisphere in the American and Asian sectors. We note that other previous studies did not consider comprehensive analysis of large-scale TIDs over the Asian sector. Equatorward large-scale TIDs from either hemisphere have been understood to interfere and continue to propagate with unchanged velocity (e.g., Balthazor & Moffett, 1997; Pradipita et al., 2016), which has also been seen in our analysis over the American sector. Overall, the estimated velocities of the equatorward large-scale TIDs on 17 March 2015 are mostly in agreement with previous studies during the same storm period (Borries et al., 2016; Zakharenkova et al., 2016). A highlight of this study is the observation of downward vertical propagation in altitudinal N_e profiles from ionosonde data during

periods when meridional propagation of large-scale TIDs was present in GNSS TEC data. At the same time, the ionosonde results coincided with in situ N_e changes from SWARM data, a possible confirmation that TIDs contributed to vertical N_e distribution all the way to topside ionosphere.

Acknowledgments
GNSS data were obtained from African Reference Frame, AFREF (ftp://ftp.afrefdata.org), IGS (ftp://garner.ucsd.edu/pub/rinex), University Navstar Consortium, UNAVCO (ftp://data-out.unavco.org), Nigerian GPS network (http://server.nignet.net/data/), the South African National Geospatial Information (ftp://ftp.trignet.co.za), and the Brazilian Network for Continuous GPS Monitoring, RBMC (ftp://geoftp.ibge.gov.br/informacoes_sobre_posicionamento_geodesico/rbmc/dados/). Magnetometer data are accessible from http://www.intermagnet.org/, http://magnetometers.bc.edu, and http://lisn.igp.gob.pe/. JULIA data were obtained from jro.igp.gob.pe. Data for solar wind parameters are available from the Web omniweb.gsfc.nasa.gov. The quiet and disturbed periods of March 2015 were accessed on http://wdc.kugi.kyoto-u.ac.jp/qddays/index.html. E. Y.'s work has been partially supported by AFOSR (FA9550-12-1-0437 and FA9550-15-1-0399) and NSF-AGS145136 grants. M. B. M. was partially supported by the NSF grant AGS-1450512.

References

Anderson, D., Anghel, A., Yumoto, K., Ishitsuka, M., & Kudeki, E. (2002). Estimating daytime vertical $E \times B$ drift velocities in the equatorial F-region using ground-based magnetometer observations. *Geophysical Research Letters*, *29*(12), 1596. https://doi.org/10.1029/2001GL014562

Astafyeva, E., Zakharenkova, I., & Förster, M. (2015). Ionospheric response to the 2015 St. Patrick's Day storm: A global multi-instrumental overview. *Journal of Geophysical Research: Space Physics*, *120*, 9023–9037. https://doi.org/10.1002/2015JA021629

Balthazor, R. L., & Moffett, R. J. (1997). A study of atmospheric gravity waves and traveling ionospheric disturbances at equatorial latitudes. *Annales de Geophysique*, *15*, 1048–1056.

Blanc, M., & Richmond, A. D. (1980). The ionospheric disturbance dynamo. *Journal of Geophysical Research*, *85*, 1669–1686.

Borries, C., Jakowski, N., & Wilken, V. (2009). Storm induced large scale TIDs observed in GPS derived TEC. *Annales de Geophysique*, *27*, 1605–1612.

Borries, C., Mahrous, A. M., Ellahouny, N. M., & Badeke, R. (2016). Multiple ionospheric perturbations during the Saint Patrick's Day storm 2015 in the European-African sector. *Journal of Geophysical Research: Space Physics*, *121*, 11,333–11,345. https://doi.org/10.1002/2016JA023178

Buchert, S., Zangerl, F., Sust, M., André, M., Eriksson, A., Wahlund, J.-E., & Opgenoorth, H. (2015). SWARM observations of equatorial electron densities and topside GPS track losses. *Geophysical Research Letters*, *42*, 2088–2092. https://doi.org/10.1002/2015GL063121

Carter, B. A., Yizengaw, E., Pradipita, R., Retterer, J. M., Groves, K., Valladares, C., … Zhang, K. (2016). Global equatorial plasma bubble occurrence during the 2015 St. Patrick's Day storm. *Journal of Geophysical Research: Space Physics*, *121*, 894–905. https://doi.org/10.1002/2015JA022194

Chau, J. L., & Woodman, R. F. (2004). Daytime vertical and zonal velocities from 150-km echoes: Their relevance to F-region dynamics. *Geophysical Research Letters*, *31*, L17801. https://doi.org/10.1029/2004GL020800

Chimonas, G (1969). The upper atmosphere in motion: The equatorial electrojet as a source of long period traveling ionospheric disturbances. *Geophysical Monograph Series*, *18*, 698–706.

Davis, M. (1971). On polar substorms as the source of large-scale traveling ionospheric disturbances. *Journal of Geophysical Research*, *76*(19), 4525–4533.

Ding, F., Wan, W., Ning, B., & Wang, M. (2007). Large-scale traveling ionospheric disturbances observed by GPS total electron content during the magnetic storm of 29–30 October 2003. *Journal of Geophysical Research*, *112*, A06309. https://doi.org/10.1029/2006JA012013

Ding, F., Wan, W., Ning, B., Zhao, B., Lin, Q., Wang, Y., … Xiong, B. (2013). Observations of poleward-propagating large-scale traveling ionospheric disturbances in Southern China. *Annals of Geophysics*, *31*, 377–385.

Drob, D. P., Emmert, J. T., Crowley, G., Picone, J. M., Shepherd, G. G., Skinner, W., … Vincent, R. A. (2008). An empirical model of the Earth's horizontal wind fields: HWM07. *Journal of Geophysical Research*, *113*, A12304. https://doi.org/10.1029/2008JA013668

Fagundes, P., Cardoso, F. A., Fejer, B. G., Venkatesh, K., Ribeiro, B. A. G., & Pillat, V. G. (2016). Positive and negative GPS-TEC ionospheric storm effects during the extreme space weather event of March 2015 over the Brazilian sector. *Journal of Geophysical Research: Space Physics*, *121*, 5613–5625. https://doi.org/10.1002/2015JA022214

Fejer, B. G., & Scherliess, L. (1998). Mid- and low-latitude prompt ionospheric zonal plasma drifts. *Geophysical Research Letters*, *25*(16), 3071–3074.

Figueiredo, C. A. O. B., Wrasse, C. M., Takahashi, H., Otsuka, Y., Shiokawa, K., & Barros, D. (2017). Large-scale traveling ionospheric disturbances observed by GPS dTEC maps over North and South America on Saint Patrick's Day storm in 2015. *Journal of Geophysical Research: Space Physics*, *122*, 4755–4763. https://doi.org/10.1002/2016JA023417

Fuller-Rowell, T. J., Codrescu, M. V., Moffett, R. J., & Quegan, S. (1994). Response the thermosphere and ionosphere to geomagnetic storms. *Journal of Geophysical Research*, *99*(A3), 3893–3914.

Georges, T. M., & Hooke, W. H. (1970). Wave-induced fluctuations in ionospheric electron content: A model indicating some observational biases. *Journal of Geophysical Research*, *75*(31), 6295–6308.

Habarulema, J. B., Katamzi, Z. T., & Yizengaw, E. (2015). First observations of poleward large-scale traveling ionospheric disturbances over the African sector during geomagnetic storm conditions. *Journal of Geophysical Research: Space Physics*, *120*, 6914–6929. https://doi.org/10.1002/2015JA021066

Habarulema, J. B., Katamzi, Z. T., Yizengaw, E., Yamazaki, Y., & Seemala, G. (2016). Simultaneous storm time equatorward and poleward large-scale TIDs on a global scale. *Geophysical Research Letters*, *43*, 6678–6686. https://doi.org/10.1002/2016GL069740

Hajkowicz, L. A., & Hunsucker, R. D. (1987). A simultaneous observation of large-scale periodic TIDs in both hemispheres following an onset of auroral disturbances. *Planet Space Science*, *35*(6), 785–791.

Hines, C. O. (1960). Internal atmospheric gravity waves at ionospheric heights. *Canadian Journal of Physics*, *38*(11), 1441–1481.

Hocke, K., & Schlegel, K. (1996). A review of atmospheric gravity waves and traveling ionospheric disturbances. *Annales Geophysicae*, *14*, 917–940.

Huang, C. M., Richmond, A. D., & Chen, M.-Q. (2005). Theoretical effects of geomagnetic activity on low-latitude electric fields. *Journal of Geophysical Research*, *110*, A05312. https://doi.org/10.1029/2004JA010994

Huang, X., & Reinisch, B. W. (1996). Vertical electron density profiles from the digisonde network. *Advances in Space Research*, *18*, 121–129.

Katamzi, Z. T., & Habarulema, J. B. (2014). Traveling ionospheric disturbances observed at South African midlatitudes during the 29–31 October 2003 geomagnetically disturbed period. *Advances in Space Research*, *53*(1), 48–62.

Kelley, M. C., Fejer, B. G., & Gonzalez, C. A. (1979). An explanation for anomalous equatorial ionospheric electric field associated with a northward turning of the interplanetary magnetic field. *Geophysical Research Letters*, *6*, 301–304.

Kuai, J., Liu, L., Liu, J., Sripathi, S., Zhang, B., Chen, Y., … Hu, L. (2016). Effects of disturbed electric fields in the low-latitude and equatorial ionosphere during the 2015 St. Patrick's Day storm. *Journal of Geophysical Research: Space Physics*, *121*, 9111–9126. https://doi.org/10.1002/2016JA022832

Knudsen, W. (1969). Neutral atmosphere wave generation by the equatorial electrojet. *Journal of Geophysical Research*, *74*(16), 4191–4192.

Lu, G., Richmond, A. D., Roble, R. G., & Emery, A. (2001). Coexistence of ionospheric positive and negative storm phases under northern winter conditions: A case study. *Journal of Geophysical Research*, *106*(A11), 24493–24504.

Matsushita, S., & Campbell, W. H. (1972). Lunar semidiurnal variations of the geomagnetic field determined from the 2.5-min data scalings. *Journal of Atmospheric and Solar-Terrestrial Physics*, *34*(7), 1187–1200.

Nava, B., Rodriguez-Zuluaga, J., Alazo-Cuartas, K., Kashcheyev, A., Migoya-Orue, Y., Radicella, S. M., … Fleury, R. (2016). Middle- and low-latitude ionosphere response to 2015 St. Patrick's Day geomagnetic storm. *Journal of Geophysical Research: Space Physics*, *121*, 3421–3438. https://doi.org/10.1002/2015JA022299

Nayak, C., Tsai, L.-C., Su, S.-Y., Galkin, I. A., Tan, A. T. K., Nofri, E., & Jamjareegulgarn, P. (2016). Peculiar features of the low-latitude and midlatitude ionospheric response to the St. Patrick's Day geomagnetic storm of 17 March 2015. *Journal of Geophysical Research: Space Physics*, *121*, 7941–7960. https://doi.org/10.1002/2016JA022489

Ngwira, C. M., McKinnell, L.-A., Cilliers, P. J., & Yizengaw, E. (2012). An investigation of ionospheric disturbances over South Africa during the magnetic storm on 15 May 2005. *Advances in Space Research*, *49*, 327–335.

Nicolls, M. J., Kelley, M. C., Coster, A. J., González, S., & Makela, J. (2004). Imaging the structure of a large-scale TID using ISR and TEC data. *Geophysical Research Letters*, *31*, L09812. https://doi.org/10.1029/2004GL019797

Prölss, G. W., & Jung, M. J. (1978). Travelling atmospheric disturbances as a possible explanation for daytime positive storm effects of moderate duration at middle latitudes. *Journal of Atmospheric and Terrestrial Physics*, *40*(12), 1354–1354.

Pradipita, R., Valladares, C. E., Carter, B. A., & Doherty, P. H. (2016). Interhemispheric propagation and interactions of auroral traveling ionospheric disturbances near the equator. *Journal of Geophysical Research: Space Physics*, *121*, 2462–2474. https://doi.org/10.1002/2015JA022043

Ramsingh, S., Sripathi, S., Sreekumar, S., Banola, S., Emperumal, K., Tiwari, P., & Kumar, B. S. (2015). Low-latitude ionosphere response to super geomagnetic storm of 17/18 March 2015: Results from a chain of ground-based observations over Indian sector. *Journal of Geophysical Research: Space Physics*, *120*, 10,864–10,882. https://doi.org/10.1002/2015JA021509

Rastogi, R. G., & Klobuchar, J. A. (1990). Ionospheric electron content within the equatorial F_2 layer anomaly belt. *Journal of Geophysical Research*, *95*(A11), 19,045–19,052.

Reinisch, B. W., & Huang, X. (1983). Automatic calculation of electron density profiles from digital ionograms: 3. Processing of bottomside ionograms. *Radio Science*, *18*(4), 477–492.

Shiokawa, K., Otsuka, Y., Ogawa, T., Balan, N., Igarashi, K., Ridley, J., … Yumoto, K. (2002). A large-scale traveling ionospheric disturbance during the magnetic storm of 15 September 1999. *Journal of Geophysical Research*, *107*(A6), 1088. https://doi.org/10.1029/2001JA000245

Thome, G. (1968). Long-period waves generated in the polar ionosphere during the onset of magnetic storms. *Journal of Geophysical Research*, *73*(69), 6319–6336.

Tsugawa, T., Saito, A., Otsuka, Y., & Yamamoto, M. (2003). Damping of large-scale traveling ionospheric disturbances detected with GPS networks during the geomagnetic storm. *Journal of Geophysical Research*, *108*(A3), 1127. https://doi.org/10.1029/2002JA009433

Tsugawa, T., Saito, A., & Otsuka, Y. (2004). A statistical study of large-scale traveling ionospheric disturbances using the GPS network in Japan. *Journal of Geophysical Research*, *109*, A06302. https://doi.org/10.1029/2003JA010302

van de Kamp, M., Pokhotelov, D., & Kauristie, K. (2014). TID characterised using joint effort of incoherent scatter radar and GPS. *Annales de Geophysique*, *32*, 1511–1532.

van Velthoven, P. F. J. (1990). Medium scale irregularities in the ionospheric electron content (PhD thesis). Netherlands: Eindhoven University of Technology.

Valladares, C. E., & Chau, J. L. (2012). The low-latitude ionosphere sensor network: Initial results. *Radio Science*, *47*, RS0L17. https://doi.org/10.1029/2011RS004978

Valladares, C. E., Villalobos, J., Hei, M. A., Sheehan, R., Basu, S., MacKenzie, E., … Rios, V. H. (2009). Simultaneous observation of traveling ionospheric disturbances in the Northern and Southern Hemispheres. *Annales de Geophysique*, *27*, 1501–1508.

Yamazaki, Y., & Maute, A. (2016). Sq and EEJ—A review on the daily variation of the geomagnetic field caused by ionospheric dynamo currents. *Space Science Reviews*. https://doi.org/10.1007/s11214-016-0282-z

Yizengaw, E., Moldwin, M. B., Zesta, E., Biouele, C. M., Damtie, B., Mebrahtu, A., … Stoneback, R. (2014). The longitudinal variability of equatorial electrojet and vertical drift velocity in the African and American sectors. *Annales de Geophysique*, *32*, 231–238.

Yizengaw, E., & Moldwin, M. B. (2009). African Meridian B-field Education and Research (AMBER) array. *Earth Moon Planet*, *104*, 237–246. https://doi.org/10.1007/s11038-008-9287-2

Yizengaw, E., Moldwin, M. B., Mebrahtu, A., Damtie, B., Zesta, E., Valladares, C. E., & Doherty, P. H. (2011). Comparison of storm time equatorial ionospheric electrodynamics in the African and American sectors. *Journal of Atmospheric and Solar-Terrestrial Physics*, *73*(1), 156–163.

Yizengaw, E., Zesta, E., Moldwin, M. B., Damtie, B., Mebrahtu, A., Valladares, C. E., & Pfaff, R. F. (2012). Longitudinal differences of ionospheric vertical density distribution and equatorial electrodynamics. *Journal of Geophysical Research: Space Physics*, *117*, A07312. https://doi.org/10.1029/2011JA017454

Zakharenkova, I., Astafyeva, E., & Cherniak, I. (2016). GPS & GLONASS observations of large-scale traveling ionospheric disturbances during the 2015 St. Patrick's Day storm. *Journal of Geophysical Research: Space Physics*, *121*, 12,138–12,156. https://doi.org/10.1002/2016JA023332